International Journal of Nanomedicine

Dovepress

open access to scientific and medical research

Open Access Full Text Article

ORIGINAL RESEARCH

Exploring the Interaction of Cobalt Oxide Nanoparticles with Albumin, Leukemia Cancer Cells and Pathogenic Bacteria by Multispectroscopic, Docking, Cellular and Antibacterial Approaches

This article was published in the following Dove Press journal:
International Journal of Nanomedicine

Niloofar Arsalan,[1,*] Elahe Hassan Kashi,[2,*] Anwarul Hasan,[3,4] Mona Edalat Doost,[5] Behnam Rasti,[6] Bilal Ahamad Paray,[7] Mona Zahed Nakhjiri,[1] Soyar Sari,[2] Majid Sharifi,[8] Koorosh Shahpasand,[9] Keivan Akhtari,[10] Setareh Haghighat,[5] Mojtaba Falahati[8]

[1]Department of Biology, Faculty of Basic Sciences, Lahijan Branch, Islamic Azad University (IAU), Lahijan, Guilan, Iran; [2]Department of Cellular and Molecular Biology, Faculty of Advanced Sciences and Technology, Tehran Medical Sciences, Islamic Azad University, Tehran, Iran; [3]Department of Mechanical and Industrial Engineering, College of Engineering, Qatar University, Doha 2713, Qatar; [4]Biomedical Research Centre, Qatar University, Doha 2713, Qatar; [5]Department of Microbiology, Faculty of Advanced Sciences and Technology, Tehran Medical Sciences, Islamic Azad University, Tehran, Iran; [6]Department of Microbiology, Faculty of Basic Sciences, Lahijan Branch, Islamic Azad University (IAU), Lahijan, Guilan, Iran; [7]Department of Zoology, College of Science, King Saud University, Riyadh 11451, Saudi Arabia; [8]Department of Nanotechnology, Faculty of Advanced Sciences and Technology, Tehran Medical Sciences, Islamic Azad University, Tehran, Iran; [9]Department of Stem Cells and Developmental Biology, Cell Science Research Center, Royan Institute for Stem Cell Biology and Technology (RI-SCBT), Tehran, Iran; [10]Department of Physics, University of Kurdistan, Sanandaj, Iran

*These authors contributed equally to this work

Correspondence: Mojtaba Falahati; Anwarul Hasan
Email mojtaba.falahati@alumni.ut.ac.ir; ahasan@qu.edu.qa

Aim: The interaction of NPs with biological systems may reveal useful details about their pharmacodynamic, anticancer and antibacterial effects.

Methods: Herein, the interaction of as-synthesized Co_3O_4 NPs with HSA was explored by different kinds of fluorescence and CD spectroscopic methods, as well as molecular docking studies. Also, the anticancer effect of Co_3O_4 NPs against leukemia K562 cells was investigated by MTT, LDH, caspase, real-time PCR, ROS, cell cycle, and apoptosis assays. Afterwards, the antibacterial effects of Co_3O_4 NPs against three pathogenic bacteria were disclosed by antibacterial assays.

Results: Different characterization methods such as TEM, DLS, zeta potential and XRD studies proved that fabricated Co_3O_4 NPs by sol-gel method have a diameter of around 50 nm, hydrodynamic radius of 177 nm with a charge distribution of −33.04 mV and a well-defined crystalline phase. Intrinsic, extrinsic, and synchronous fluorescence as well as CD studies, respectively, showed that the HSA undergoes some fluorescence quenching, minor conformational changes, microenvironmental changes as well as no structural changes in the secondary structure, after interaction with Co_3O_4 NPs. Molecular docking results also verified that the spherical clusters with a dimension of 1.5 nm exhibit the most binding energy with HSA molecules. Anticancer assays demonstrated that Co_3O_4 NPs can selectively lead to the reduction of K562 cell viability through the cell membrane damage, activation of caspase-9, -8 and -3, elevation of Bax/Bcl-2 mRNA ratio, ROS production, cell cycle arrest, and apoptosis. Finally, antibacterial assays disclosed that Co_3O_4 NPs can stimulate a promising antibacterial effect against pathogenic bacteria.

Conclusion: In general, these observations can provide useful information for the early stages of nanomaterial applications in therapeutic platforms.

Keywords: cobalt oxide, nanoparticle, synthesis, spectroscopy, docking, anticancer, antibacterial

Introduction

Nanotechnology is one of the key infrastructures of the current scientific-industrial revolution and will help the development of science and technology for the next decades.[1,2] Combination of nanotechnology and other domains will result in the

potential advancement of technology in the future.[2,3] One of the implications of nanotechnology is the ability to produce smart materials that could be of potential assistant in development of bio-smart devices.[4,5] It clearly shows that the fabrication and advancement of nano-based systems should be among the top priorities of every country.[6] In the field of pharmacy, nanotechnology has provided very fundamental applications and the strategic goal in this field is patient-centered design and disease-driven, smart and targeted drugs.[7–10] These nano-based systems show specific potency and ability to sense the damaged environment in the tissue and to decide how to control the pharmacodynamic and pharmacokinetic of nano-drugs.[11–13] These drugs will not be activated if they do not meet the requirements for their implementation.[14] The nature of such drugs is to accurately predict their function, a property which is not present in current approaches. The application of nanotechnology in medicine in relation to the timely identification and promising treatment of cancer is the focus of research activities worldwide.[15,16] Nanotechnology can provide emergence of fundamental changes in how to deal with the approaches to potentially treat cancer.[17,18]

On another side, the overuse of antibiotics to kill the bacteria has made them resistant to antibiotics and spread infectious diseases.[19] Therefore, it is essential to look for new antibacterial substances (new generation of antibacterial drugs) to prevent the growth of bacteria. Silver,[20,21] gold[22,23] and platinum[24,25] nanoparticles (NPs) exhibit significant antibacterial activity. This property is due to the extremely small size and surface-to-volume ratio of these particles.[26] Therefore, due to the high antibacterial activity of the NPs, they can be used to enhance the safety of food packaging[27,28] as well as in the development of a new generation of antibacterial drugs.[29,30] In this area, cobalt oxide (Co_3O_4) NPs have shown outstanding features because of their promising physicochemical properties like the anisotropy constant, coercivity and Curie temperature, saturation magnetization and ease of fabrication.[31] The Co_3O_4 NPs have been reported to be applied in different medical applications such as cancer therapy,[32,33] magnetic resonance imaging (MRI),[34,35] and targeted drug delivery.[36,37]

However, before introducing NPs as anticancer or antibacterial agents, their effects on the biological systems like the structure of proteins should be considered.[38,39] Among the proteins, human serum albumin (HSA) is the most widely studied biomolecules and provides wide applications in biochemistry, biophysics and pharmacology.[40] HSA is the most abundant protein present in plasma and carries many drugs/NPs for various therapeutic demands. HSA also transports hormones, fatty acids and other compounds, and maintains osmotic pressure and regulate the blood pH.[41,42] Because of the properties that albumin demonstrates in binding to ligands, it is used as a circulating reservoir for many metabolites.[43] The interaction of proteins with different ligands plays an essential role in biological processes.[44,45] The most important application of predicting protein-NPs interactions is to design novel nano-drug-based carriers.[46,47] Biophysical and bioinformatical methods such as calorimetry, spectroscopy and dynamic studies are commonly used to study the interaction of proteins and NPs.[44] As a result of the use of biophysical and computer-based techniques, the interaction of NPs with proteins can be investigated before experimental testing, and after selecting compounds that are more likely to bind to the target, they can be tested in the laboratory or in vivo.[48,49]

Therefore, in this study, the interaction of as-fabricated Co_3O_4 NPs with HSA was studied by different kinds of spectroscopic methods as well as in silico studies. The anticancer effects of Co_3O_4 NPs on leukemia K562 cells were also investigated by different cellular and molecular assays. Finally, the antibacterial effects of Co_3O_4 NPs against three pathogenic bacteria, ie *Escherichia coli* (ATCC 25922), *Pseudomonas aeruginosa* (ATCC 27853) and *Staphylococcus aureus* (ATCC 25923) were explored.

Materials

HSA, $Co(NO_3)_2.6H_2O$, 1-anilino-8-naphthalene sulfonate (ANS), and 3-(4,5-dimethylthiazol-2-yl)-2,5-diphenyltetrazolium bromide (MTT) were purchased from Sigma-Aldrich Co. (NY, USA). All chemicals used in experiments were of analytical grade.

Synthesis of Co_3O_4 NPs

The fabrication of Co_3O_4 NPs was done based on sol-gel method. In the first step, 1.5 g of $Co(NO_3)_2.6H_2O$ and 3 gr of sodium hydroxide (NaOH) were dissolved in 50 mL double distilled water and ethanol, respectively and continuous stirring was carried out for 20 min. The NaOH solution was then mixed into the $Co(NO_3)_2.6H_2O$ dropwise with a continuous stirring at ambient temperature for 4 hr to form light pink coloured precipitates, followed by washing and drying at 150°C for 4 hr. Finally, calcination was done at 800°C for 2 hr.

Characterization of Co_3O_4 NPs

The size and morphology of as prepared Co_3O_4 NPs were characterized by TEM investigation (EM10C, 100 kV, Zeiss, Germany). The crystalline structure of synthesized NPs was examined using X-ray defecation (XRD) (Philips PW 1730, Amsterdam, Netherlands). The hydrodynamic and zeta potential values of NPs were also determined using dynamic light scattering (DLS) [Brookhaven instruments 90Plus particle size/zeta analyzer (Holtsville, NY, USA)].

Preparation of Co_3O_4 NPs and HSA Solutions

HSA molecules were solubilized in phosphate buffer (pH 7.4, 10 mM) and the concentration was estimated using Beer-Lambert law at 280 nm. The as-synthesized Co_3O_4 NPs were also dissolved in phosphate buffer (pH 7.4, 10 mM), vortexed for 30 min, and sonicated at 50°C for 20 min.

Fluorescence Spectroscopy Study

Employing a spectrofluorometer (Carry model, Varian, Australia), the intrinsic and ANS fluorescence spectroscopy studies were done to reveal the thermodynamic parameters of the interaction between HSA and Co_3O_4 NPs, and conformational changes of HSA, respectively. The Co_3O_4 NPs with varying concentrations (1–50 μg/mL) of Co_3O_4 NPs were added into HSA solution (0.1 μg/mL). The emission intensity of HSA molecules both alone and with Co_3O_4 NPs was detected at an excitation wavelength of 280 nm with a slit width of 10 nm and emission wavelength of 310–450 nm with a slit width of 10 nm.

For ANS fluorescence study, the protein samples in the absence and presence of Co_3O_4 NPs were added by ANS solution (20 μM) and the excitation was done at 380 nm with a slit width of 10 nm. All reported signals were corrected against fluorescence intensities of buffer and Co_3O_4 NPs solutions as well as inner filter effects. Synchronous fluorescence study was also done at $\Delta\lambda$ = 20 nm and $\Delta\lambda$ = 60 nm to detect the microenvironmental changes of Tyr and Trp residues, respectively. The experimental setup was similar to intrinsic fluorescence study.

Docking Study

The Molecular docking study was done by using HEX 6.3 software (http://hex.loria.fr). The 3D X-ray crystallographic structure of HSA (PDB ID: 1AO6) was downloaded from the online Protein Data Bank RCSB PDB (http://www.pdb.org). The cluster of Co_3O_4 NPs was designed on Avogadro software. Different Co_3O_4 nanoclusters with varying dimension and morphologies were developed to study the interactions of Co_3O_4 NPs with HSA molecule.

Circular Dichroism Study

The secondary structural changes of the HSA (0.2 μg/mL) in the presence of varying concentrations (1–50 μg/mL) of Co_3O_4 NPs were evaluated by analyzing CD signals on spectropolarimeter (Aviv model 215, Lakewood, NJ, USA) in a wavelength range of 190–260 nm at a scan rate of 20 nm/min at 298 K. Each signal was subtracted from the control samples and the data were reported as the mean residue ellipticity (MRE in deg cm^2 $dmol^{-1}$), based on the following equation:[45]

$$\mathrm{MRE} = \mathrm{Observed\,CD\,(mdeg)/Cp \times n \times l \times 10} \quad (1)$$

where n is the number of residues, l is the path length of the light, and C_p is the HSA concentration. Helicity content was then estimated from the MRE values at 222 nm using the following equation:[45]

$$\alpha - \mathrm{helix}(\%) = -(\mathrm{MRE222} - 2340)/30300 \times 100 \quad (2)$$

Cell Culture

The human leukemia cell line (K562) was purchased from the Pasteur Institute of Tehran (Iran). The fresh lymphocytes were prepared using gradient centrifugation on Ficoll-Paque PLUS (Sigma, USA) based on the Ethics approved by the Ethics Committee of the Tehran Medical Sciences, Islamic Azad University (Tehran, Iran). The cells were grown in RPMI-1640 medium added by 10% FBS, 100 μg/mL streptomycin and 100 μg/mL penicillin at 37°C in a 5% CO_2 humidified atmosphere.

MTT Assay

The cells were seeded in 96-well plates and added by varying concentrations (1–200 μg/mL) of Co_3O_4 NPs for 24 hr. After preparation of the cells for MTT assay, the solution was added for 4 hr at 37°C followed by addition of DMSO for 2 min. Optical density of the control and treated samples was detected at 570 nm using an ELISA reader (Expert 96, Asys Hitch, Ec Austria).

LDH and Caspase-8, 9, 3 Assays

The K562 cell membrane damage induced by varying concentrations (1–200 μg/mL) of Co_3O_4 NPs after 24 hr was

assessed using lactate dehydrogenase (LDH) as a biomarker, according to the manufacturer's protocols (LDH Assay Kit/(Colorimetric) (ab102526), Cambridge, UK). The caspases-8, 9, 3 activities of K562 cells, incubated with IC_{50} concentration of Co_3O_4 NPs after 24 hr, were evaluated employing the Apo Target™ Caspase Colorimetric Sampler Kit (Invitrogen Life Technologies; Carlsbad, CA, USA), based on the manufacturer's protocols.

Real-Time PCR Assay

The upregulation or downregulation of Bax mRNA and Bcl-2 mRNA was examined by quantitative Realtime PCR (qPCR) based on our previous reports [49, 50]. The primers for GAPDH mRNA, Bcl-2 mRNA and Bax mRNA were as following: FW; ACACCCACTCCTCCAC CTTTG, REV; TCCACCACCCTGTTGCTGTAG, FW; AACGTGCCTCATGAAATAAAG, REV; TTATTGGATG TGCTTTGCATTC, FW; GGGTGGTTGGGTGAGACTC, REV; AGACACGTAAGGAAAACGCATTA.

ROS, Cell Cycle and Apoptosis Assays

The DCF intensity, the population of cells in different stages of cell cycle and the percentage of apoptotic cells in K562 cells after treatment with the IC_{50} concentration of Co_3O_4 NPs for 24 hr were determined by DCFDA-Cellular ROS Assay Kit (ab113851), Propidium Iodide (PI) Flow Cytometry Kit for Cell Cycle Analysis (ab139418), and Annexin V-FITC Apoptosis Staining/Detection Kit (ab14085), respectively, based on the manufacturer's protocols.

Agar Well Diffusion Method

Escherichia coli (ATCC 25922), *Pseudomonas aeruginosa* (ATCC 27853) and *Staphylococcus aureus* (ATCC 25923) were cultured in LB broth followed by coating over the agar plate. Standard-sized wells were punched on Nutrient Agar and different concentrations of Co_3O_4 NPs (200–1.6 µg/mL) were added to each well for 24 hr. The diameter of inhibitory zones, minimum inhibitory concentration (MIC), and minimum bactericidal concentration (MBC) was then measured.

Statistical Analyses

The data were produced in triplicate and analyzed by one-way analysis of variance (ANOVA) and statistical significance was specified by means of SPSS software.

Results

Characterization of Co_3O_4 NPs

The Co_3O_4 NPs were synthesized by sol-gel method and characterized by different approaches such as TEM, DLS, zeta potential, and XRD analysis. As shown in Figure 1A, the synthesized NPs have an almost homogenous spherical structures with an average diameter of around 50 nm. DLS study displayed that the hydrodynamic radius of fabricated NPs is 177 nm (Figure 1B). Charge distribution measurements revealed a relatively high zeta potential value of around −33.04 mV (PDI= 0.251) on the NP surface. Although, the synthesized NPs showed a tendency to aggregate based on TME image, DLS and zeta potential data indicated that the synthesized NPs have a high colloidal stability. Indeed, the process of sample preparation for TEM images due to dried state of NPs often results in the formation of NP aggregates. XRD analysis (Figure 1C) and corresponding data (Figure 1D) also revealed a crystalline phase of synthesized Co_3O_4 NPs, which is in agreement with already published pattern.[50]

Fluorescence Study

Intrinsic fluorescence study was done to detect the probable conformational changes of HSA molecules around aromatic residues after interaction with different concentrations (1, 10, 20, 50 µg/mL) of Co_3O_4 NPs. As shown in Figure 2A, it can be observed that the interaction of Co_3O_4 NPs with HSA molecules results in the fluorescence quenching of receptor, and the quenching is more significant in the case of higher concentrations of Co_3O_4 NPs. Furthermore, the well-known Stern-Volmer equation was used to determine the Stern-Volmer constant (K_{SV}) value. Based on Figure 2A, the K_{SV} value was determined to be 0.037 mL/µg.

ANS fluorescence study was carried out to determine the possible denaturation of HSA molecules after interaction with various concentrations of Co_3O_4 NPs. As depicted in Figure 2B, it can be revealed that Co_3O_4 NPs resulted in the quaternary structural changes of HSA in a dose-dependent manner. To more discuss the microenvironmental changes around the aromatic residues in the HSA structure after interaction with Co_3O_4 NPs, the synchronous fluorescence spectroscopy was done. As demonstrated in Figure 2C and D, the $\Delta\lambda$ = 60 nm and $\Delta\lambda$ = 20 nm were fixed to reveal the microenvironmental changes of Trp and Tyr residues, respectively. It was revealed that after addition of varying concentrations of Co_3O_4 NPs, there is no significant red or blue shift in the detected spectra of Trp residues, however, the resultant

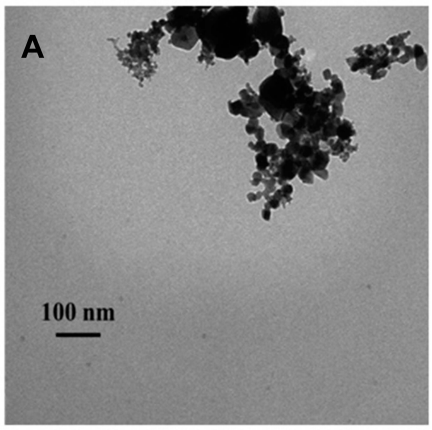

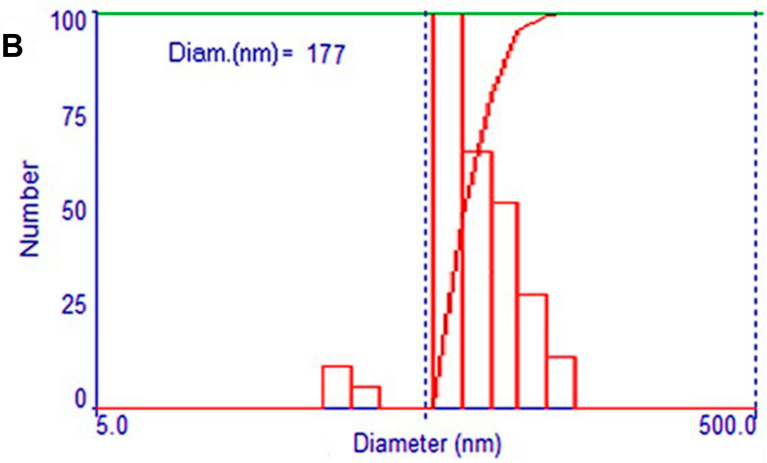

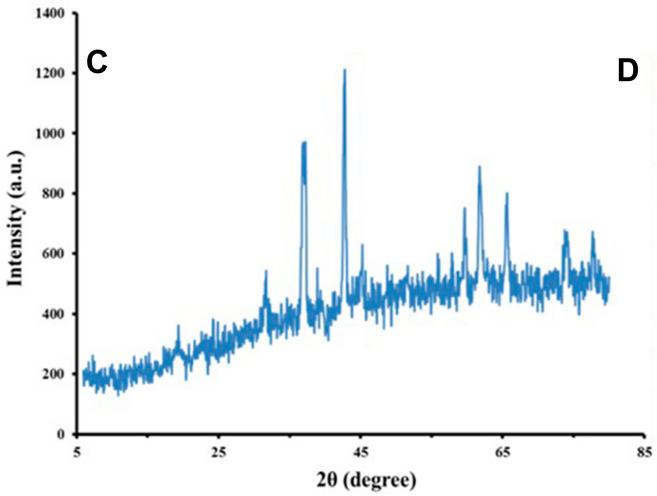

D

Pos. [°2θ]	Height [cts]	FWHM Left [°2θ]	d-spacing [Å]	Rel. Int [%]
19.30539	52.22195	1.1808	4.59779	6.57
31.69253	109.0773	1.1808	2.82335	13.72
36.86117	588.7966	0.1968	2.43847	74.03
37.23083	612.5602	0.1968	2.41511	77.02
42.74577	795.3021	0.2952	2.11542	100
59.66258	223.4041	0.5904	1.54978	28.09
61.82127	394.5702	0.492	1.50057	49.61
65.59132	317.3445	0.3936	1.42333	39.9
73.98947	169.6766	0.5904	1.28118	21.33

Figure 1 (**A**) TEM images, (**B**) DLS histogram, (**C**) XRD pattern, and (**D**) XRD data of synthesized Co_3O_4 NPs by sol-gel method.

spectra of Tyr residues showed a significant red shift, suggesting the displacement of these residues to a polar microenvironment.

Molecular Docking Study

The molecular docking study was run with the different dimensions (r=0.5 nm, r=1 nm, r=1, 1.5 nm, r=2 nm) of spherical Co_3O_4 clusters and one of the HSA chains and the resulting binding sites are shown in Figure 3A–D, respectively. The resulting binding energies are summarized in Table 1. It was observed that the binding energies of spherical Co_3O_4 clusters with dimensions of r=0.5 nm, r=1 nm, r=1, 1.5 nm, and r=2 nm and HSA molecules were −210.58, −242.86, −614.58, and −586.14 E-values, respectively. Therefore, it can be determined the highest binding energy was between spherical Co_3O_4 cluster with a size of 1.5 nm and HSA molecule as a receptor. The visualization of the docked pose and involving residues within 4 Å for different Co_3O_4 clusters (Figure 4A–D) and HSA molecule was performed using CHIMERA (www.cgl.ucsf.edu/chimera) and Pymol (http://pymol.sourceforge.net/) tools. As summarized in Table 1, it can be expressed that the contributing residues of HSA upon interaction with spherical Co_3O_4 cluster with a size of 1.5 nm are Ser-435, Lys-439, Phe-395, Glu-396, Glu-400, Gly-399, Leu-398, Tyr-401, Lys-402, Lys-519, Gln-522, Glu-518, Ala-176, Pro-180, Glu-184. In this binding site, 5 hydrophobic residues, 3 polar residues, and 7 electrostatic residues are involved, showing that the electrostatic bonds are the main contributing forces upon the interaction of Co_3O_4 cluster (1.5 nm) with HSA in receptor binding site. Moreover, it can be observed that Tyr-401 is located in the binding pose of protein after interaction with Co_3O_4 cluster (1.5 nm), which is in good agreement with synchronous fluorescence data.

Circular Dichroism Study

Far UV-circular dichroism (CD) study was performed to quantify the secondary structural changes of HSA after

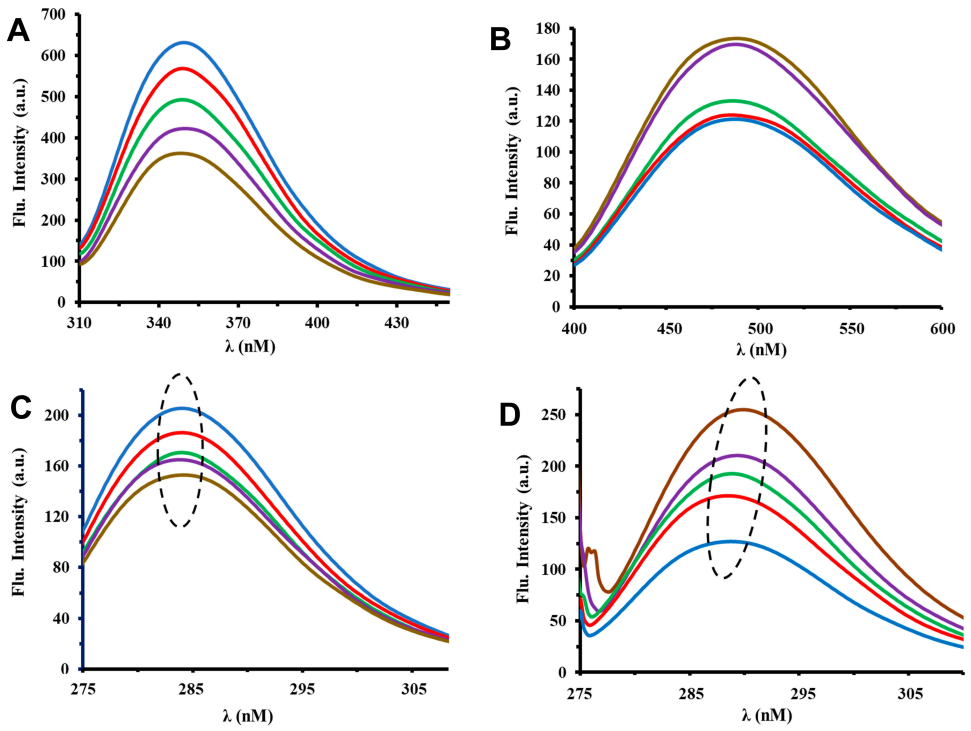

Figure 2 (**A**) Intrinsic fluorescence, (**B**) ANS fluorescence, (**C**) synchronous fluorescence study at $\Delta\lambda$ = 60 nm, and (**D**) synchronous fluorescence study at $\Delta\lambda$ = 20 nm of HSA after interaction with different concentrations [0 μg/mL (blue), 1 μg/mL (red), 10 μg/mL (green), 20 μg/mL (purple), 50 μg/mL (brown)] of Co_3O_4 NPs. The dotted circle shows the red or blue shift in the $\lambda_{max.}$

interaction with different concentrations (1, 10, 20, 50 μg/mL) of Co_3O_4 NPs. As shown in Figure 5A, the CD spectrum of HSA shows two minima at 208 and 222 nm, indicating the native helical structure of HSA. Furthermore, it was depicted that after addition of varying concentrations of Co_3O_4 NPs, the positions of CD spectra were almost unchanged, suggesting the preserve of the native structure of HSA even in the presence of high concentrations of Co_3O_4 NPs. To more discuss about the secondary structural changes of HSA molecules in the presence of varying concentrations of Co_3O_4 NPs, CDDN software was used to quantify the amount of α-helix, β-sheets and random coil structures. As shown in Figure 5B, it can be detected that the amount of α-helix structure reduces to 88%, whereas the amounts of β-sheets and random coil structures increase to 105% and 108%, respectively, in the presence of 50 μg/mL of Co_3O_4 NPs. These data suggest that Co_3O_4 NPs did not substantially change the secondary structures of HSA even at high concentrations.

MTT Assay

The K562 cells and lymphocytes were incubated with Co_3O_4 NPs at the concentrations of 0, 10, 50, 100, and 200 μg/mL for 24 hr and the cell viability was explored employing MTT assay. It was determined that Co_3O_4NPs up to the concentrations of 50 μg/mL and 200 μg/mL did not induce remarkable reduction in cell viability of K562 cells and lymphocyte, respectively. In the case of K562 cells, as the concentration of the Co_3O_4NPs increased from 50 to 200 μg/mL, reduction in cell viability was determined to happen in a more significant and a dose-dependent manner.

The MTT assay indicated that cell viability decreased to 97.46%, 95.65%, 83.10%, and 73.31% (*P<0.05) when lymphocyte was incubated with Co_3O_4 NPs at the concentrations of 10, 50, 100, and 200 μg/mL, respectively (Figure 6A). However, it was shown that the cell viability was reduced to 95.75%, 78.27% (*P<0.05), 61.85% (*P<0.05), 40.58% (*P<0.01) when the K562 cells were incubated with the above-mentioned concentrations of Co_3O_4 NPs (Figure 6A), which determined that these NPs can selectively stimulate a decrease in the cell viability of cancer cells. It was also determined that the IC_{50} concertation of Co_3O_4 NPs in lymphocyte and K562 cells is around>200 μg/mL and 142 μg/mL, respectively.

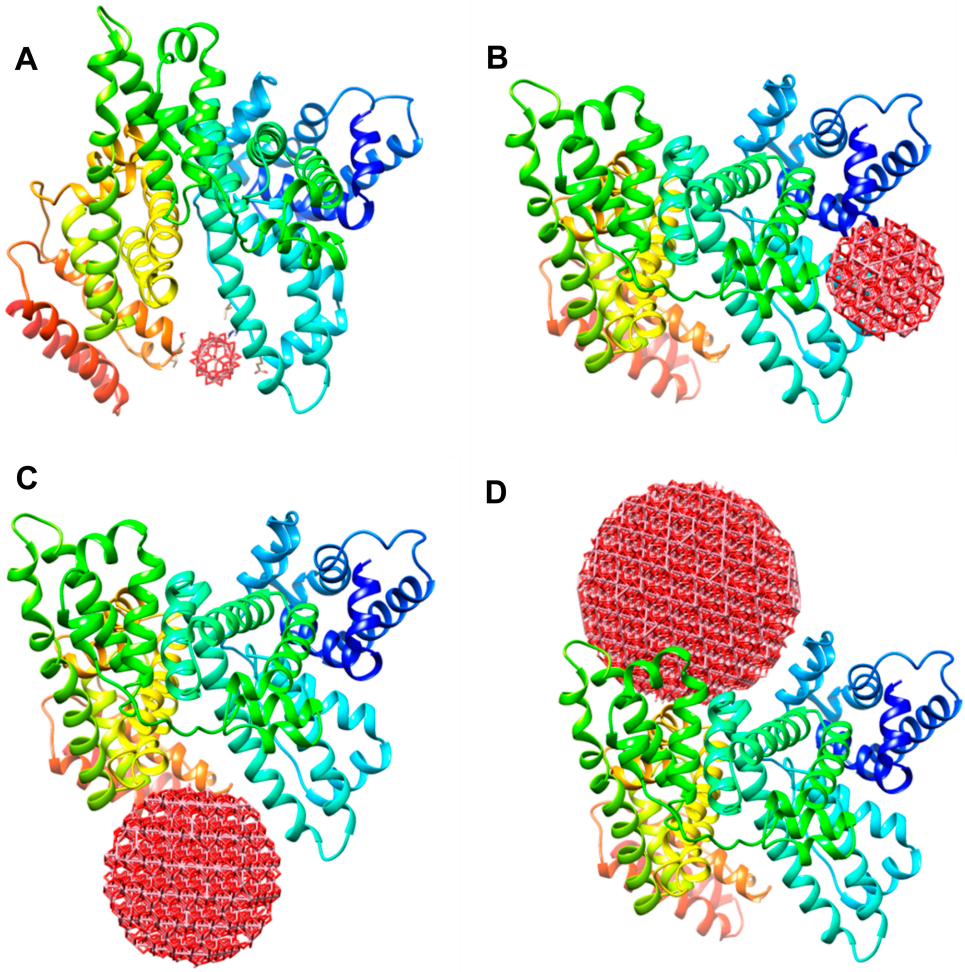

Figure 3 HEX 6.3 outcomes of the interaction of HSA with spherical Co_3O_4 nanoclusters, (**A**) r=0.5 nm, (**B**) r=1 nm, (**C**) r=1.5 nm, (**D**) r =2 nm.

LDH Release Assay

Any damage to cell membrane integrity results in the release of LDH into cell culture medium and the degree of its extracellular activity depends on the cytotoxicity of the nanomaterials. In this assay, it was shown that Co_3O_4 NPs increase LDH activity in extracellular medium of K562 cells in a dose-dependent fashion (Figure 6B). The LDH assay displayed that LDH release increased to

Table 1 Docking Results of Spherical Co_3O_4 Clusters with HSA Molecule

Dimensions	Docking Score (E-value)	Residue Interacted
r=0.5 nm	−210.58	Thr-515, Leu-516, Ser-517, Glu-119, Arg-117, Val-116
r=1 nm	−242.86	Lys-159, Glu-17, Asn-18, Gly-15, Leu-14, Lys-12, Asp-13, Leu-284, Leu-283, Lys-286, Pro-282, Glu-280, Leu-283
r=1.5 nm	−614.58	Ser-435, Lys-439, Phe-395, Glu-396, Glu-400, Gly-399, Leu-398, Tyr-401, Lys-402, Lys-519, Gln-522, Glu-518, Ala-176, Pro-180, Glu-184
r=2 nm	−486.14	Lys-93, Asp-89, Glu-86, Glu-97, Glu-100, Gln-104, His-105, Thr-467, Lys-466, Pro-468, Glu-465, Asp-471, Thr-474, Thr-478, Glu-479, Gln-204, Lys-205, Lys-475

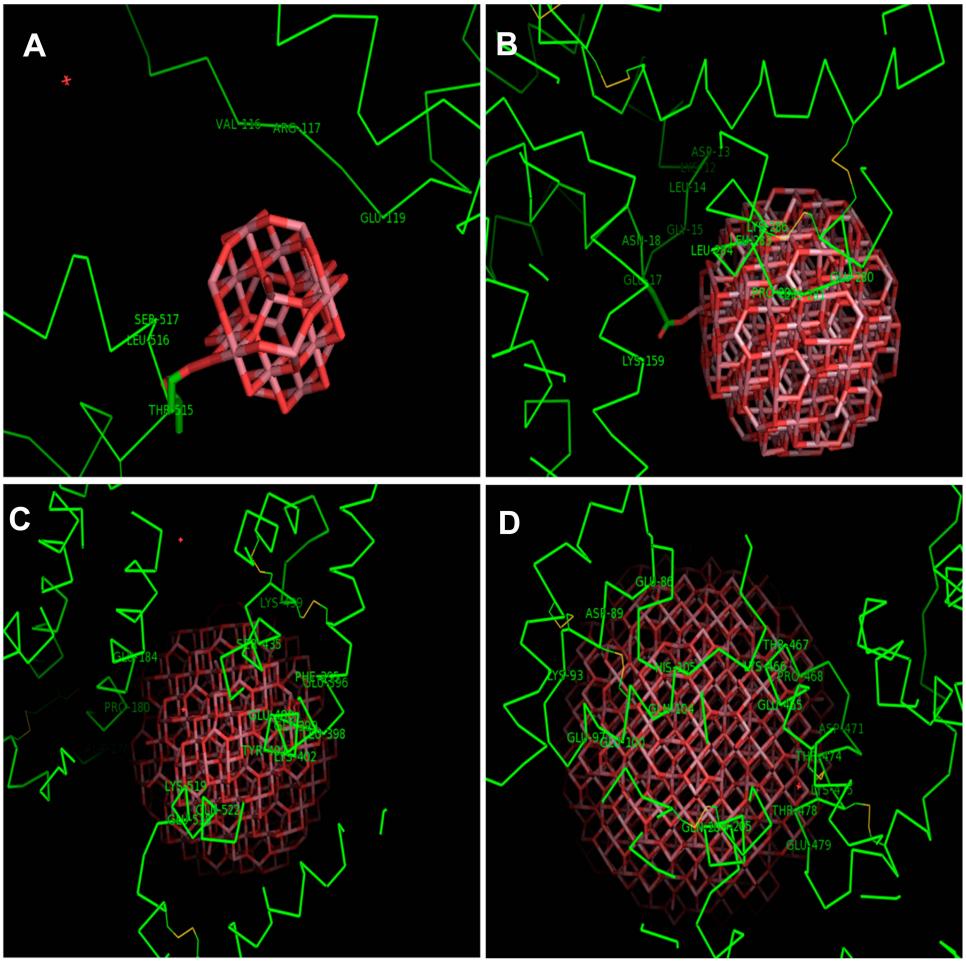

Figure 4 The resulting docking pose of HSA after interaction with spherical Co_3O_4 nanoclusters, (**A**) r=0.5 nm, (**B**) r=1 nm, (**C**) r=1.5 nm, (**D**) r =2 nm.

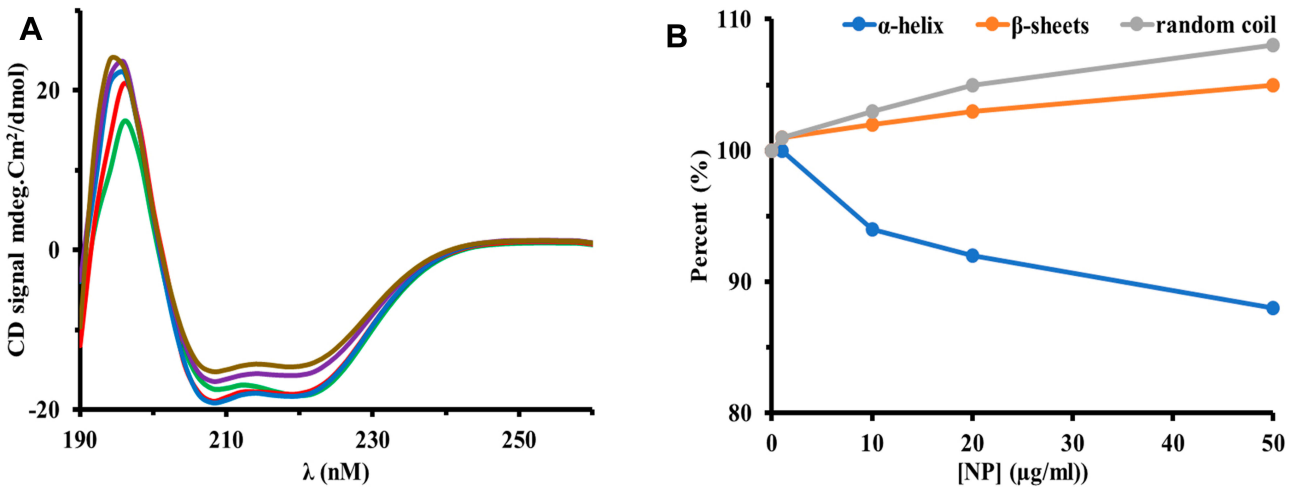

Figure 5 (**A**) CD spectra, (**B**) quantified CD data of HSA after interaction with different concentrations [0 μg/mL (blue), 1 μg/mL (red), 10 μg/mL (green), 20 μg/mL (purple), 50 μg/mL (brown)] of Co_3O_4 NPs.

101.05%, 107.28%, 161.22% (*P<0.05), and 239.47% (**P<0.01) when K562 cells were incubated by Co_3O_4 NPs at the concentrations of 10, 50, 100, and 200 μg/mL for 24 hr, respectively (Figure 6B). Therefore, it can be indicated that there is a significant positive correlation between LDH activity and MTT assay.

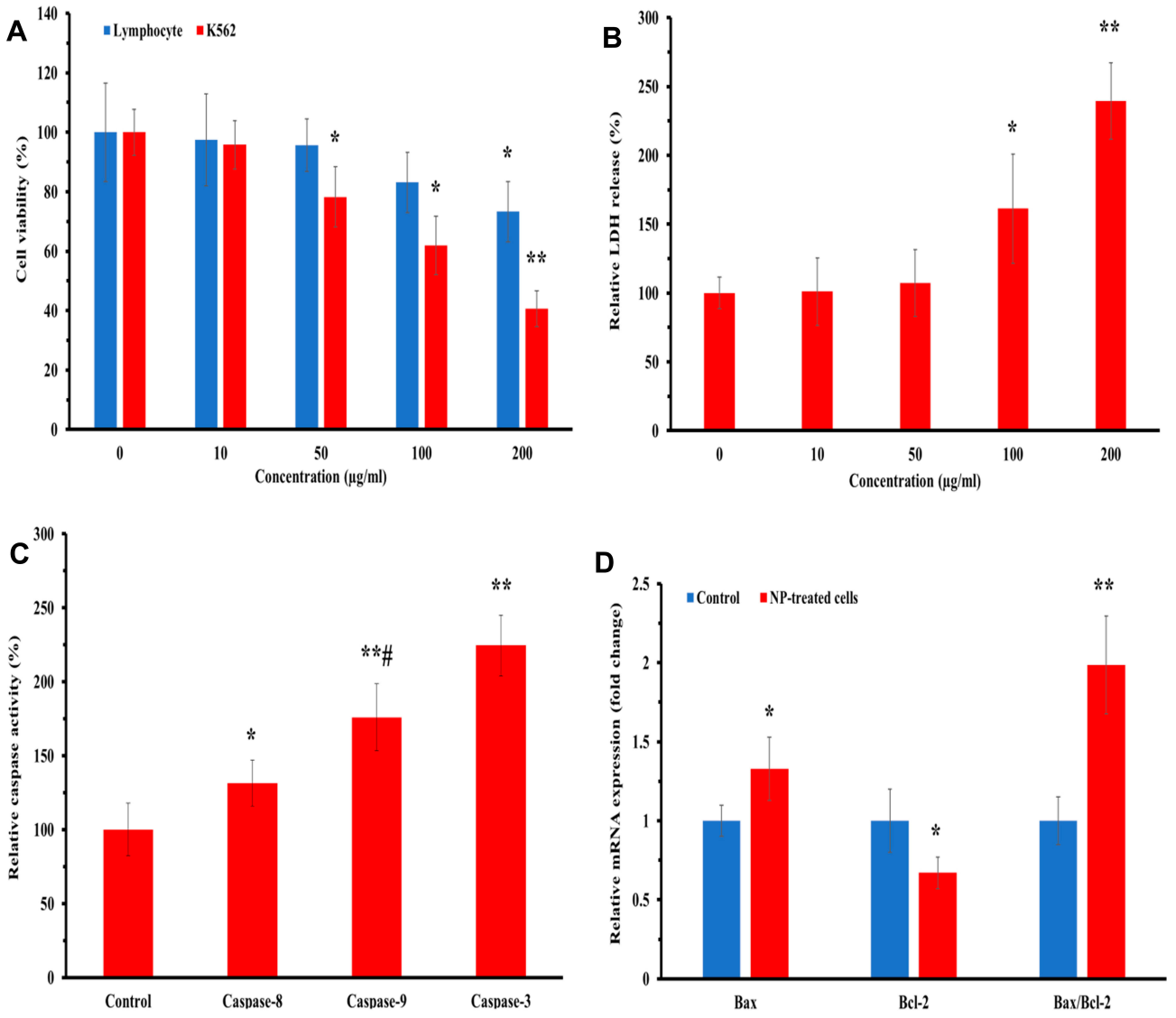

Figure 6 (**A**) MTT assay of lymphocytes and K562 cells incubated with different concentrations of Co_3O_4 NPs, (**B**) LDH assay of K562 cells incubated with different concentrations of Co_3O_4 NPs, (**C**) caspase assay of K562 cells incubated with IC50 concentrations of Co_3O_4 NPs, (**D**) qPCR assay of K562 cells incubated with IC50 concentrations of Co_3O_4 NPs. *P<0.5 and **P<0.01 relative to negative untreated cells. #P<0.5 relative to the activity of caspase-8.

Caspase Assay

The activities of caspase-8, 9 and 3 were assessed in the K562 cells treated with IC_{50} concentration Co_3O_4 NPs (142 µg/mL) for 24 hr to reveal the mechanism of apoptosis. The activation of caspase-8 and caspase-9 demonstrates the extrinsic and intrinsic-mediated pathways of apoptosis, respectively. As shown in Figure 6C, it was demonstrated that the activity of caspase-8 (*P<0.05), caspase-9 (**P<0.01) and caspase-3 (**P<0.01) were significantly increased in NP-treated groups relative to untreated cells. However, the increase in the activation of caspase-9 was more remarkable (#P<0.05) than the activation of caspase-8 in NP-treated cells, indicating the dominant role of intrinsic-mediated pathway of apoptosis.

Molecular Study

qPCR study was carried out to analyze the mRNA levels of apoptotic gene, Bax and antiapoptotic gen, Bcl-2 in K562 cells exposed to IC_{50} concentration Co_3O_4 NPs (142 µg/mL) for 24 hr. It was exhibited that IC_{50} concentration Co_3O_4 NPs significantly induced the upregulation of Bax mRNA (*P<0.05) and downregulation of Bcl-2 mRNA (Figure 6D). Indeed, it was shown that the expression ratio of Bax/Bcl-2 mRNA was significantly (*P<0.05) increased in the NP-treated K562 cells compared to that of the control cells. It can be suggested that the Co_3O_4 NPs can stimulate apoptosis in K562 cells through mitochondria-mediated pathways which is in agreement with caspase assay outcome.

ROS Generation

The elevation of ROS level in cells due to the presence of NPs has been indicated as signaling pathways involved in the initiation and execution of apoptosis. The quantitative analysis (Figure 7) revealed that the IC_{50} concentration of Co_3O_4 NPs (142 µg/mL) after 24 hr triggered intracellular ROS production in K562 cells. Figure 7A shows that the mean DCF fluorescence intensity of control cells is about 209 unit; however, this amount increases to 1911 unit (Figure 7B) after incubation of K562 cells with IC_{50} concentration of Co_3O_4 NPs for 24 hr. This increase in DCF fluorescence intensity can indicate a significant (***P< 0.001) production of ROS inside the treated cells (Figure 7C).

Cell Cycle Assay

The cell cycle assay was explored to evaluate the population of K562 cells in each phase of cell cycle in the presence of Co_3O_4 NPs. Figure 8A and B show the cell cycle diagrams of control K562 cells and treated K562 cells with IC_{50} concentration of Co_3O_4 NPs after 24 hr. As shown in Figure 8C, the population of cells in G_0 in the case of control cells is 13.7%. However, addition of Co_3O_4 NPs to K562 cells result in a significant (*P<0.05) increase in the population of cells in G_o phase, indicating the initiation of apoptosis (Figure 8C). The data also depicted that the number of cells in S phase significantly (*P<0.05) increase in NP-treated group compared to the control cells, determining the cell cycle arrest in the S phase.

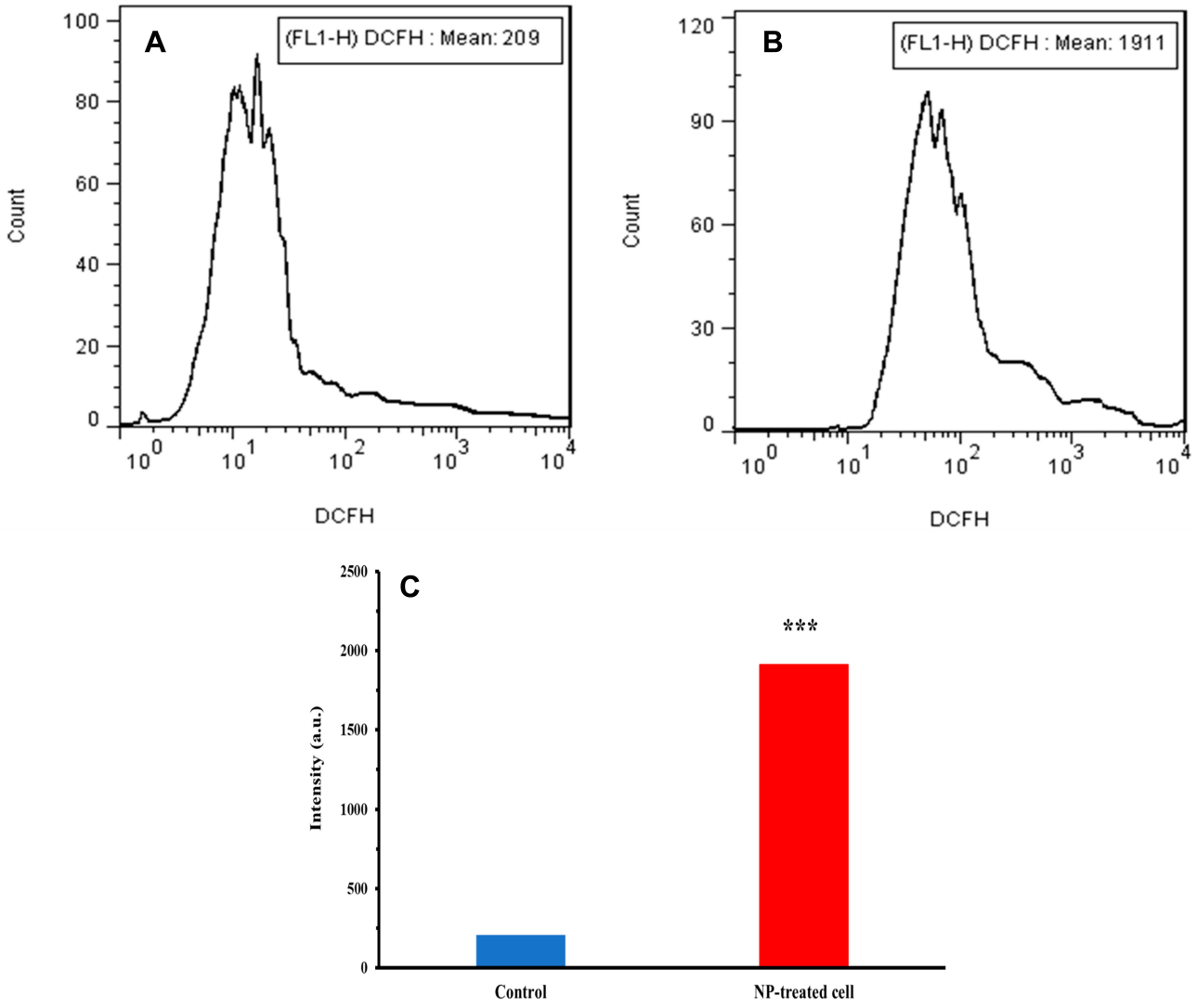

Figure 7 ROS assay of (**A**) control K562 cells, (**B**) treated K562 cells incubated with IC50 concentrations of Co_3O_4 NPs, (**C**) statistical analysis histogram. ***P<0.01 relative to negative untreated cells.

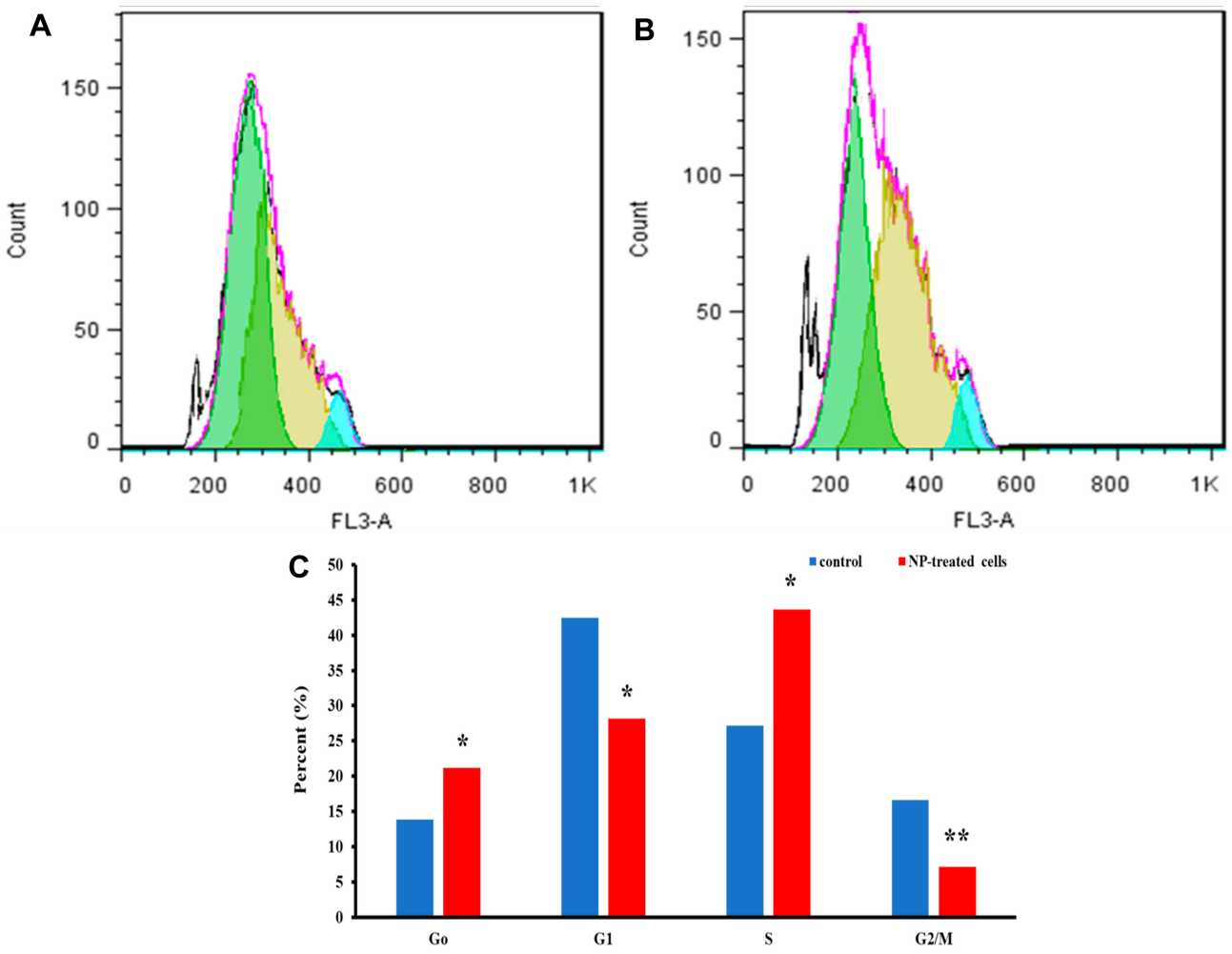

Figure 8 Cell cycle assay of (**A**) control K562 cells, (**B**) treated K562 cells incubated with IC50 concentrations of Co_3O_4 NPs, (**C**) statistical analysis histogram. *P<0.5 and **P<0.01 relative to negative untreated cells.

Furthermore, the population of cells in G2/M phase significantly (**P<.0.01) reduces after incubation of cells with IC_{50} concentration of Co_3O_4 NPs compared to the control sample (Figure 8C), suggesting the inhibition of cell division. This outcome determined that Co_3O_4 NPs can reduce the proliferation of K562 cell through cell cycle arrest and induction of apoptosis.

Apoptosis and Necrosis Assay

The K562 cells were incubated by IC_{50} concentration of Co_3O_4 NPs (142 µg/mL) for 24 hr, and the quantity of apoptotic and necrotic cells was determined by flow cytometry assay. Figure 9A and B display the representative flow cytometry outcomes of control and NP-treated cells, respectively. As exhibited in Figure 9C, the percentage of viable cells (Q4), apoptotic cells (Q2, Q3), and necrotic cells (Q1) in NP-treated cells are different from those of untreated cells. It was shown that the percentage of viable cells significantly (**P<0.01) decreased from 86.6% in control cells to 32% in NP-treated cells, whereas the percentage of apoptotic cells are remarkable (***P<0.001) in NP-treated group compared to that of control cells. However, it was displayed that the percentage of necrotic cells was almost similar in the case of both untreated and NP-treated cells. Therefore, it may be indicated that Co_3O_4 NPs induce a significant cytotoxicity against K562 cells through apoptosis.

Antibacterial Activities of Synthesized Co_3O_4 NPs

The antibacterial activities of synthesized Co_3O_4 NPs are depicted in Figure 10. The outcomes demonstrated that the synthesized Co_3O_4 NPs induced significant antibacterial activity against studied pathogenic bacteria. Table 2 also

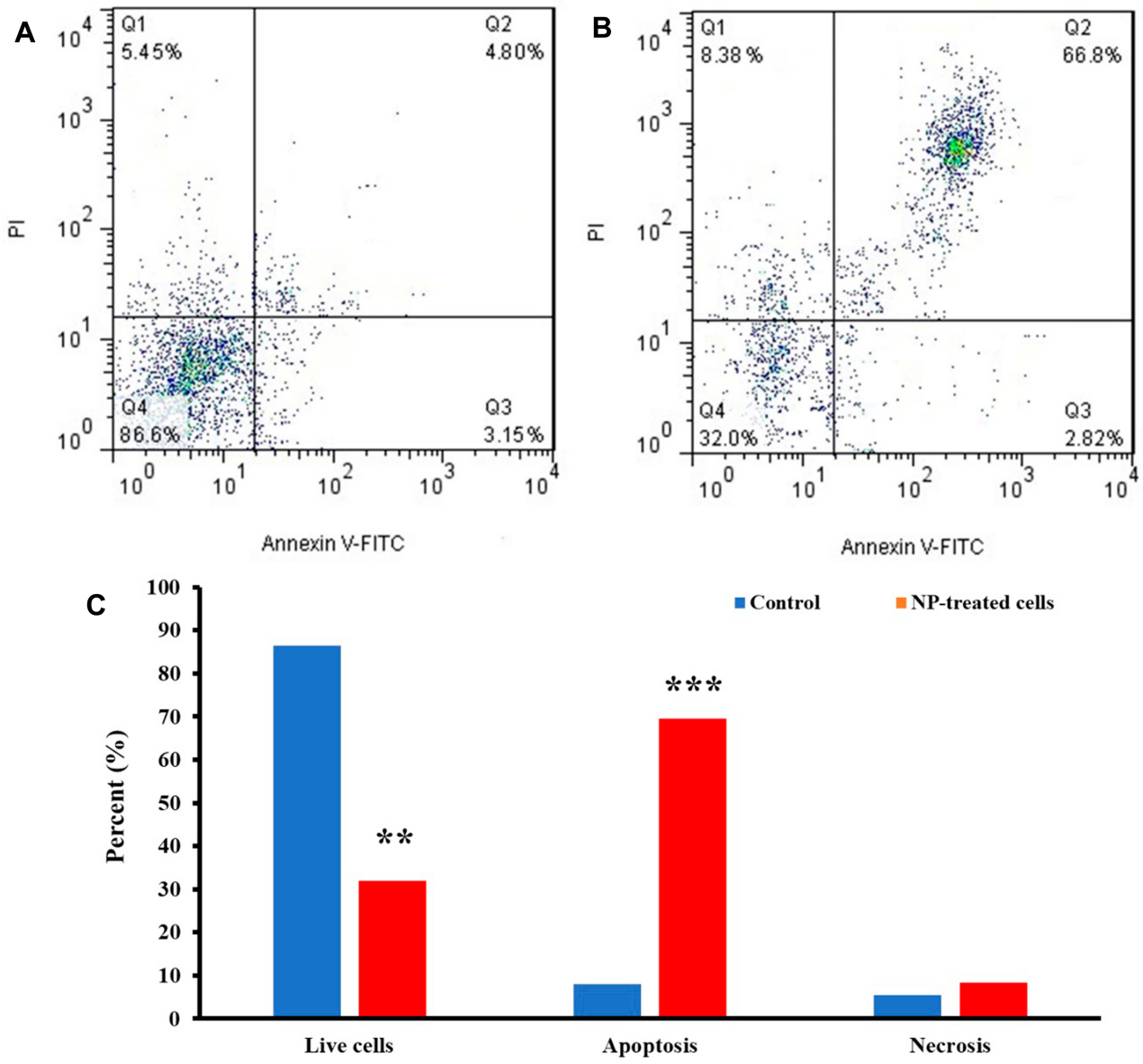

Figure 9 Annexin-PI assay of (**A**) control K562 cells, (**B**) treated K562 cells incubated with IC50 concentrations of Co_3O_4 NPs, (**C**) statistical analysis histogram. **P<0.1 and ***P<0.001 relative to negative untreated cells.

summarizes the inhibition zone diameters of synthesized Co_3O_4 NPs against *S. aureus, E. coli* and *P. aeruginosa* bacterial strains, showing the antibacterial effects in a dose-dependent manner.

MIC and MBC Methods

The antibacterial activity of Co_3O_4 NPs was further explored using MIC and MBC methods. As shown in Table 3, the Co_3O_4 NPs displayed a pronounced antibacterial activity against both Gram-positive and Gram-negative pathogenic bacteria even at very low concentrations. However, these NPs were most effective against *E. coli* compared to the other pathogenic bacteria.

Discussion

Due to the importance of metal NPs in the anticancer and antibacterial activities, special attention should be paid to optimizing their production with uniformed size and shapes. Numerous studies have been conducted to control the synthesis of Co_3O_4 NPs,[51–53] and the present study is highly consistent with the previous results. Herein, the XRD pattern results show that Co_3O_4 NPs are well

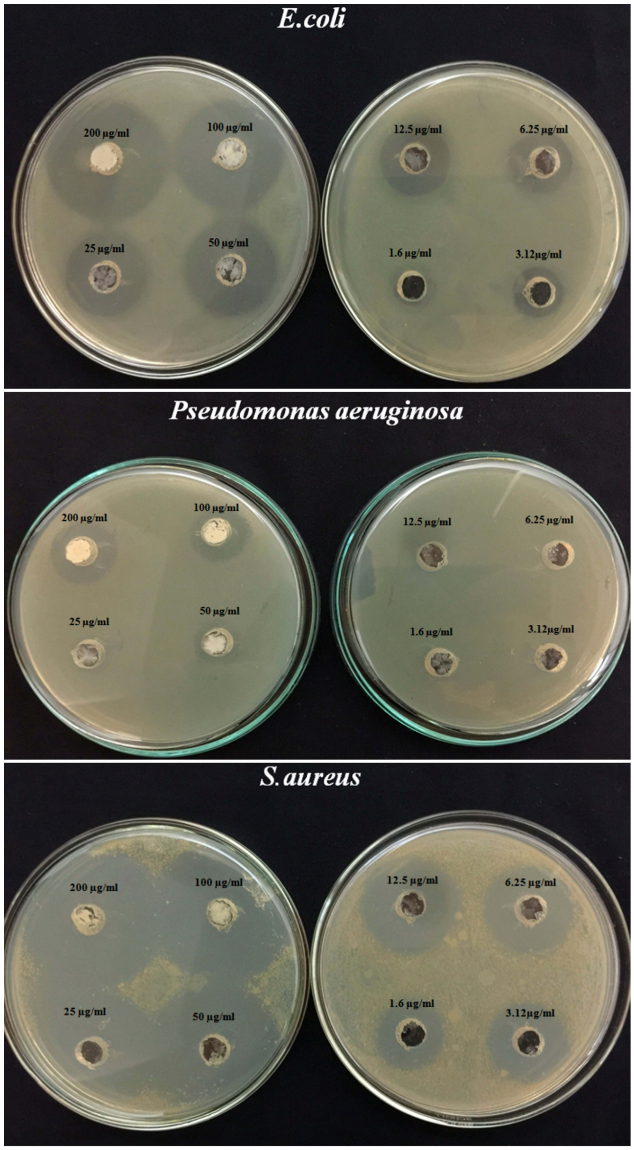

Figure 10 Visible zone formed by different concentrations (200–3.12µg/mL) of Co_3O_4 NPs against *S. aureus*, *E. coli* and *P. aeruginosa*.

crystallized which is consistent with the previous models of Liang et al,[54] Khan et al,[52] Chattopadhyay et al,[55] and Rahimi-Nasrabadi et al.[50] The pattern illustrates the pure structure of Co_3O_4 NPs synthesized by the sol-gel method. In addition, the results of the TEM and DLS show that the size and the structure of Co_3O_4 NPs are uniformly fabricated.

Since Co_3O_4 NPs exhibit high oxidation potential in the extracellular medium,[56] the interaction of Co_3O_4 NPs and HSA is predictable due to the existence of diverse HSA domains with oxidation and reduction properties.[57] Hydrophobic segments of HSA are known as interacting domains which are highly potent to interact with metallic

Table 2 Average Inhibition Zone of Synthesized Co_3O_4 NPs Against Pathogenic Bacteria

Bacteria	Concentration (µg/mL)	Inhibition Zone (mm)
S. aureus	200	45±0.5
	100	42±0.5
	50	40±0.5
	25	38±0.5
	12.5	32±0.5
	6.25	29±0.5
	3.12	25±0.5
	1.6	22±0.5
E. coli	200	38±0.5
	100	35±0.5
	50	31±0.5
	25	26±0.5
	12.5	20±0.5
	6.25	18±0.5
	3.12	15±0.5
	1.6	11±0.5
P. aeruginosa	200	20±0.5
	100	18±0.5
	50	14±0.5
	25	12±0.5
	12.5	10±0.5
	6.25	–
	3.12	–
	1.6	–

NPs such as Co_3O_4.[41,56] In order to confirm the interaction of Co_3O_4 NPs and HSA, the binding of HSA to Co_3O_4 NPs was investigated by different spectroscopic methods and docking study. The fluorescence spectroscopy study revealed that the interaction of HSA and Co_3O_4 NPs caused minor structural changes in the tertiary structure of the protein, while the CD study indicated that the Co_3O_4 NPs did not alter the secondary structures of the HSA. This indicates that the lack of sufficient number of non-polar amino acids in the binding domain (Table 1) does not cause major changes in the structure of HSA. Furthermore, based on the number of residues involved in the

Table 3 MIC and MBC of Co_3O_4 NPs Against Pathogenic Bacteria

Bacteria	MIC (µg/mL)	MBC (µg/mL)
S. aureus	3.12	6.25
E. coli	1.6	3.12
P. aeruginosa	6.25	12.5

interaction, it was found that the nanoclusters with the sizes of 1.5 and 2 nm provided a higher tendency to interact with the HSA due to the much lower energy barrier. Similar to our results, Esfandfar et al[41] and Azizi et al[58] showed that, although the interaction of copper oxide NPs with HSA did not alter the secondary structure of the protein, they caused some slight changes in the tertiary structure of the protein. However, it has been shown that gold and silver NPs alter the secondary structure of albumin.[59,60] Moreover, it has been reported that copper oxide NPs[61] and cerium oxide NPs[62] have no effect on the secondary structure of the HSA. Overall, no change in the secondary structure of the HSA indicates that the protein is in a native folded structure, while the NP-induced slight structural changes can be reversible.

As reported in Figure 7, Co_3O_4 NPs cause oxidative stress due to increased intracellular ROS, as a main factor enhancing the cytotoxicity of metallic NPs on normal and cancerous cells.[63,64] However, our results showed that lymphocyte cells were more resistant to Co_3O_4-induced cytotoxicity than K562 cancerous cells. Thus, despite the negative effects of Co_3O_4 NPs on K562 cells at concentrations >100 µg/mL, Co_3O_4 NPs showed no negative effects on normal cells. On the other hand, Co_3O_4 NPs induced apoptosis in K562 cells based on the increased level of intracellular ROS, which is a crucial signal in the induction of apoptosis.[26] In addition, our results confirmed that Co_3O_4 NPs induced apoptosis in K562 cells via both intrinsic and extrinsic pathways by increasing the expression levels of Bax/Bcl-2 mRNA and activation of caspase-9, −8, and −3. In agreement with our results, Khan, Ansari, Khan, Ahmad, Al-Obaid, Al-Kattan[52] revealed that the addition of Co_3O_4 NPs increased the expression levels of Bax/Bcl-2 mRNA in cancerous cells, which eventually induced apoptotic cell death. On the other hand, it was determined that the use of Co_3O_4 NPs in addition to enhancing intrinsic-mediate pathway of apoptosis, induced cell mortality by activation of caspase-8 as a marker of extrinsic pathway of apoptosis.[55] Thus, despite the uncertainty in the mechanism of toxicity of Co_3O_4 NPs against the control and cancerous cells, this study emphasizes that the optimum concentrations of Co_3O_4 NPs which is between 50 and 100 µg/mL can control and inhibit the proliferation of K562 cells growth without adverse effects on normal cells. Similar to our findings, Chattopadhyay et al[55] exhibited that high concentrations of Co_3O_4 NPs have toxic effects on natural cells, whereas a decrease in concentration can provide a platform for drug delivery to cancerous cells in addition to reducing toxicity. It has also been reported that Co_3O_4 NPs cause cell mortality by increasing ROS and an anti-inflammatory cytokine response.[65] Furthermore, in a cellular model, Khan et al[52] described that controlled concentration of Co_3O_4 NPs (<80 µg/mL) had no negative effect on normal cells in addition to reducing the proliferation of human colorectal cancer cells.

On the other side, the antibacterial assay showed that Co_3O_4 NPs caused a significant antibacterial effect on both Gram-positive and Gram-negative bacterial strains. However, the most antibacterial effect of Co_3O_4 NPs was observed on *S. aureus* and *E. coli*, referring to more changes in the outer membrane of Gram-positive bacteria in the presence of cobalt ions. Similar to our results, previous studies have reported the antibacterial activities of copper oxide,[66,67] cerium oxide,[62] zinc oxide[68,69] and zero-valent iron[38] NPs. In addition, Chang et al,[70] Parada et al[53] and Khan et al[52] showed that by increasing the concentration of Co_3O_4 NPs up to 200 µg/mL., the activity of both Gram-positive and Gram-negative bacteria were significantly decreased. It has also been observed that the synthesis of Co_3O_4-cellulose magnetic[71] and graphene-Co_3O_4[72] nanocomposites not only drastically reduce the activity of Gram-positive bacteria, but also they increase the antibacterial activity of cobalt by several times against Gram-negative bacteria. Although a precise antibacterial mechanism of Co_3O_4 NPs has not been well provided, it seems that production of ROS induced by cobalt ions release and associated cell membrane damage stimulated the antimicrobial activity of these NPs.

Conclusion

Although nanotechnology has many advantages and potentials, the investigation of the interaction between NPs and biological systems is a major concern. HSA as the most abundant protein in plasma with various physiological and pharmacological roles can bind to different NPs. Therefore, it is important to study the binding of small molecules like NPs to this protein. In this study, it was found that Co_3O_4 NPs induced some slight changes on the structure of HSA. Cellular studies also depicted that Co_3O_4 NPs can selectively result in reduction of K562 cell growth through both extrinsic and intrinsic apoptotic pathways. The antibacterial studies also exhibited that Co_3O_4 NPs can be used as great candidate against pathogenic bacteria. Taken together, these observations can hold a great promise for healthy and safety aspects in the early stages of nanomaterial applications.

Acknowledgment

Niloofar Arsalan and Elahe Hassan Kashi are joint first authors. This research was made possible by the grants NPRP10-120-170-211 from Qatar National Research Fund (QNRF) under Qatar Foundation and GCC-2017-005 under the GCC collaborative research Program from Qatar University. The authors would like to also extend their sincere appreciation to the Researchers Supporting Project Number (RSP- 2019/144), King Saud University, Riyadh, Saudi Arabia. The statements made herein are the sole responsibility of the authors.

Disclosure

The authors report no conflicts of interest in this work.

References

1. Zabeo A, Keisler JM, Hristozov D, Marcomini A, Linkov I. Value of information analysis for assessing risks and benefits of nanotechnology innovation. *Environ Sci Eur*. 2019;31(1):11. doi:10.1186/s12302-019-0194-0
2. Larsson S, Jansson M, Boholm Å. Expert stakeholders' perception of nanotechnology: risk, benefit, knowledge, and regulation. *J Nanopart Res*. 2019;21(3):57. doi:10.1007/s11051-019-4498-1
3. Morales AAA, Nielsen J, Gomes ER, Rasmusen LB, Bacarini H, Thomsen B. Some insights into nanotechnology innovation processes and patterns for advanced materials. *Contaduría y administración*. 2019;64(1):11.
4. Zhang H, Tian Y, Jiang L. Fundamental studies and practical applications of bio-inspired smart solid-state nanopores and nanochannels. *Nano Today*. 2016;11(1):61–81. doi:10.1016/j.nantod.2015.11.001
5. Cai P, Leow WR, Wang X, Wu YL, Chen X. Programmable nano–bio interfaces for functional biointegrated devices. *Adv Mater*. 2017;29 (26):1605529. doi:10.1002/adma.201605529
6. Dettenhofer M, Ondrejovič M, Vásáry V, et al. Current state and prospects of biotechnology in Central and Eastern European countries. Part I: visegrad countries (CZ, H, PL, SK). *Crit Rev Biotechnol*. 2019;39(1):114–136. doi:10.1080/07388551.2018.1523131
7. Truong-Dinh Tran T, Ha-Lien Tran P, Tu Nguyen K, Tran V-T. Nanoprecipitation: preparation and application in the field of pharmacy. *Curr Pharm Des*. 2016;22(20):2997–3006. doi:10.2174/1381612822666160408151702
8. Fedorov A, Yurkova M. Molecular chaperone GroEL–toward a nano toolkit in protein engineering, production and pharmacy. *Nano World J*. 2018;4(1):8–15. doi:10.17756/nwj.2018-053
9. El-Sawy HS, Al-Abd AM, Ahmed TA, El-Say KM, Torchilin VP. Stimuli-responsive nano-architecture drug-delivery systems to solid tumor micromilieu: past, present, and future perspectives. *ACS Nano*. 2018;12(11):10636–10664. doi:10.1021/acsnano.8b06104
10. Sharifi M, Attar F, Saboury AA, et al. Plasmonic gold nanoparticles: optical manipulation, imaging, drug delivery and therapy. *J Control Release*. 2019;311–312:170–189. doi:10.1016/j.jconrel.2019.08.032
11. Pawar S, Shevalkar G, Vavia P. Glucosamine-anchored doxorubicin-loaded targeted nano-niosomes: pharmacokinetic, toxicity and pharmacodynamic evaluation. *J Drug Target*. 2016;24 (8):730–743. doi:10.3109/1061186X.2016.1154560
12. Choi YH, Han H-K. Nanomedicines: current status and future perspectives in aspect of drug delivery and pharmacokinetics. *Int J Pharm Investig*. 2018;48(1):43–60. doi:10.1007/s40005-017-0370-4
13. Gamasaee NA, Muhammad HA, Tadayon E. et al. The effects of nickel oxide nanoparticles on structural changes, heme degradation, aggregation of hemoglobin and expression of apoptotic genes in lymphocytes. *J Biomol Struct Dyn*. 2019:1–11. doi:10.1080/07391102.2019.1662850
14. Cui D, Huang J, Zhen X, Li J, Jiang Y, Pu K. A semiconducting polymer nano-prodrug for hypoxia-activated photodynamic cancer therapy. *Angew Chem Int Ed*. 2019;58(18):5920–5924. doi:10.1002/anie.201814730
15. Björnmalm M, Thurecht KJ, Michael M, Scott AM, Caruso F. Bridging bio–nano science and cancer nanomedicine. *ACS Nano*. 2017;11(10):9594–9613. doi:10.1021/acsnano.7b04855
16. Zheng Y, Li Z, Chen H, Gao Y. Nanoparticle-based drug delivery systems for controllable photodynamic cancer therapy. *Eur J Pharm Sci*. 2020;144:105213. doi:10.1016/j.ejps.2020.105213
17. Ghafari M, Haghiralsadat F, Khanamani Falahati-pour S, Zavar Reza J. Development of a novel liposomal nanoparticle formulation of cisplatin to breast cancer therapy. *J Cell Biochem*. 2020;1:1–9.
18. Guo S, Vieweger M, Zhang K, et al. Ultra-thermostable RNA nanoparticles for solubilizing and high-yield loading of paclitaxel for breast cancer therapy. *Nat Commun*. 2020;11(1):1–11. doi:10.1038/s41467-020-14780-5
19. Camcioglu Y, Okur DS, Aksaray N, Darendeliler F, Hasanoglu E. Factors affecting physicians' perception of the overuse of antibiotics. *Med Mal Infect*. 2020;1:1–6.
20. Boateng J, Catanzano O. Silver and silver nanoparticle-based antimicrobial dressings. *Ther Dressings Wound Heal Appl*. 2020:157–184.
21. Gunputh UF, Le H, Lawton K, Besinis A, Tredwin C, Handy RD. Antibacterial properties of silver nanoparticles grown in situ and anchored to titanium dioxide nanotubes on titanium implant against Staphylococcus aureus. *Nanotoxicology*. 2020;14(1):97–110. doi:10.1080/17435390.2019.1665727
22. Yang X, Wei Q, Shao H, Jiang X. Multivalent aminosaccharide-based gold nanoparticles as narrow-spectrum antibiotics in vivo. *ACS Appl Mater Interfaces*. 2019;11(8):7725–7730. doi:10.1021/acsami.8b19658
23. Zhou L, Yu K, Lu F, et al. Minimizing antibiotic dosage through in situ formation of gold nanoparticles across antibacterial wound dressings: a facile approach using silk fabric as the base substrate. *J Clean Prod*. 2020;243:118604. doi:10.1016/j.jclepro.2019.118604
24. Nishanthi R, Malathi S, Palani P. Green synthesis and characterization of bioinspired silver, gold and platinum nanoparticles and evaluation of their synergistic antibacterial activity after combining with different classes of antibiotics. *Mater Sci Eng C*. 2019;96:693–707. doi:10.1016/j.msec.2018.11.050
25. Deng T, Zhao H, Shi M, et al. Photoactivated trifunctional platinum nanobiotics for precise synergism of multiple antibacterial modes. *Small*. 2019;15(46):1902647. doi:10.1002/smll.201902647
26. Sharifi M, Hosseinali SH, Saboury AA, Szegezdi E, Falahati M. Involvement of planned cell death of necroptosis in cancer treatment by nanomaterials: recent advances and future perspectives. *J Control Release*. 2019;299:121–137. doi:10.1016/j.jconrel.2019.02.007
27. Biswas MC, Tiimob BJ, Abdela W, Jeelani S, Rangari VK. Nano silica-carbon-silver ternary hybrid induced antimicrobial composite films for food packaging application. *Food Packag Shelf Life*. 2019;19:104–113. doi:10.1016/j.fpsl.2018.12.003
28. Jayakumar A, Heera K, Sumi T, et al. Starch-PVA composite films with zinc-oxide nanoparticles and phytochemicals as intelligent pH sensing wraps for food packaging application. *Int J Biol Macromol*. 2019;136:395–403. doi:10.1016/j.ijbiomac.2019.06.018
29. Wu Z, Xu H, Xie W, et al. Study on a novel antibacterial light-cured resin composite containing nano-MgO. *Colloids Surf B Biointerfaces*. 2020;188:110774. doi:10.1016/j.colsurfb.2020.110774
30. Soltani S, Akhbari K, White J. Synthesis, crystal structure and antibacterial activity of a homonuclear nickel (II) metal-organic nano supramolecular architecture. *Polyhedron*. 2020;176:114301. doi:10.1016/j.poly.2019.114301

31. Amiri S, Shokrollahi H. The role of cobalt ferrite magnetic nanoparticles in medical science. *Mater Sci Eng C*. 2013;33(1):1–8. doi:10.1016/j.msec.2012.09.003
32. Zhu H, Deng J, Yang Y, et al. Cobalt nanowire-based multifunctional platform for targeted chemo-photothermal synergistic cancer therapy. *Colloids Surf B Biointerfaces*. 2019;180:401–410. doi:10.1016/j.colsurfb.2019.05.005
33. Zhu H, Deng J, Yang Z, et al. Facile synthesis and characterization of multifunctional cobalt-based nanocomposites for targeted chemo-photothermal synergistic cancer therapy. *Compos B Eng*. 2019;178:107521. doi:10.1016/j.compositesb.2019.107521
34. Lin W-C, Chuang -C-C, Chang C-J, Chiu Y-H, Yan M, Tang C-M. The effect of electrode topography on the magnetic properties and MRI application of electrochemically-deposited, synthesized, cobalt-substituted hydroxyapatite. *Nanomaterials*. 2019;9(2):200. doi:10.3390/nano9020200
35. Lin W, Chuang C, Yao C, Tang C. Effect of cobalt precursors on cobalt-hydroxyapatite used in bone regeneration and MRI. *J Dent Res*. 2020;0022034519897006.
36. Wang G, Ma Y, Wei Z, Qi M. Development of multifunctional cobalt ferrite/graphene oxide nanocomposites for magnetic resonance imaging and controlled drug delivery. *Chem Eng J*. 2016;289:150–160. doi:10.1016/j.cej.2015.12.072
37. Dey C, Baishya K, Ghosh A, Goswami MM, Ghosh A, Mandal K. Improvement of drug delivery by hyperthermia treatment using magnetic cubic cobalt ferrite nanoparticles. *J Magn Magn Mater*. 2017;427:168–174. doi:10.1016/j.jmmm.2016.11.024
38. Anbouhi TS, Esfidvajani EM, Nemati F, et al. albumin binding, anticancer and antibacterial properties of synthesized zero valent iron nanoparticles. *Int J Nanomedicine*. 2019;14:243. doi:10.2147/IJN.S188497
39. Behzadi E, Sarsharzadeh R, Nouri M, et al. Albumin binding and anticancer effect of magnesium oxide nanoparticles. *Int J Nanomedicine*. 2019;14:257. doi:10.2147/IJN.S186428
40. Sohrabi MJ, Dehpour A-R, Attar F, et al. Silymarin-albumin nanoplex: preparation and its potential application as an antioxidant in nervous system in vitro and in vivo. *Int J Pharm*. 2019;572:118824. doi:10.1016/j.ijpharm.2019.118824
41. Esfandfar P, Falahati M, Saboury A. Spectroscopic studies of interaction between CuO nanoparticles and bovine serum albumin. *J Biomol Struct Dyn*. 2016;34(9):1962–1968. doi:10.1080/07391102.2015.1096213
42. Hassanian M, Aryapour H, Goudarzi A, Javan MB. Are Zinc oxide nanoparticles safe? A structural study on human serum albumin using in vitro and in silico methods. *J Biomol Struct Dyn*. 2020;1–6. doi:10.1080/07391102.2019.1711189
43. Shaklai N, Garlick RL, Bunn HF. Nonenzymatic glycosylation of human serum albumin alters its conformation and function. *J Biol Chem*. 1984;259(6):3812–3817.
44. Aghili Z, Taheri S, Zeinabad HA, et al. Investigating the interaction of Fe nanoparticles with lysozyme by biophysical and molecular docking studies. *PLoS One*. 2016;11(10):e0164878. doi:10.1371/journal.pone.0164878
45. Zeinabad HA, Kachooei E, Saboury AA, et al. Thermodynamic and conformational changes of protein toward interaction with nanoparticles: a spectroscopic overview. *RSC Adv*. 2016;6(107):105903–-105919. doi:10.1039/C6RA16422F
46. Hajsalimi G, Taheri S, Shahi F, Attar F, Ahmadi H, Falahati M. Interaction of iron nanoparticles with nervous system: an in vitro study. *J Biomol Struct Dyn*. 2018;36(4):928–937. doi:10.1080/07391102.2017.1302819
47. Jafari Azad V, Kasravi S, Alizadeh Zeinabad H, et al. Probing the conformational changes and peroxidase-like activity of cytochrome c upon interaction with iron nanoparticles. *J Biomol Struct Dyn*. 2017;35(12):2565–2577. doi:10.1080/07391102.2016.1222972
48. Sabziparvar N, Saeedi Y, Nouri M, et al. Investigating the interaction of silicon dioxide nanoparticles with human hemoglobin and lymphocyte cells by biophysical, computational, and cellular studies. *J Phys Chem B*. 2018;122(15):4278–4288. doi:10.1021/acs.jpcb.8b00193
49. Rahmani S, Mogharizadeh L, Attar F, Rezayat SM, Mousavi SE, Falahati M. Probing the interaction of silver nanoparticles with tau protein and neuroblastoma cell line as nervous system models. *J Biomol Struct Dyn*. 2017;21(2017):1–15.
50. Rahimi-Nasrabadi M, Naderi HR, Karimi MS, Ahmadi F, Pourmortazavi SM. Cobalt carbonate and cobalt oxide nanoparticles synthesis, characterization and supercapacitive evaluation. *J Mater Sci*. 2017;28(2):1877–1888.
51. Moradpoor H, Safaei M, Rezaei F, et al. Optimisation of cobalt oxide nanoparticles synthesis as bactericidal agents. *Open Access Maced J Med Sci*. 2019;7(17):2757. doi:10.3889/oamjms.2019.747
52. Khan S, Ansari AA, Khan AA, Ahmad R, Al-Obaid O, Al-Kattan W. In vitro evaluation of anticancer and antibacterial activities of cobalt oxide nanoparticles. *J Biol Inorg Chem*. 2015;20(8):1319–1326. doi:10.1007/s00775-015-1310-2
53. Parada J, Atria A, Wiese G, Rivas E, Corsini G. Synthesis, characterization and antibacterial activity of cobalt (Iii) complex with phenanthroline and maltose. *J Chil Chem Soc*. 2014;59(4):2636–2639. doi:10.4067/S0717-97072014000400002
54. Liang Y, Li Y, Wang H, et al. Co 3 O 4 nanocrystals on graphene as a synergistic catalyst for oxygen reduction reaction. *Nat Mater*. 2011;10(10):780–786. doi:10.1038/nmat3087
55. Chattopadhyay S, Dash SK, Tripathy S, et al. Toxicity of cobalt oxide nanoparticles to normal cells; an in vitro and in vivo study. *Chem Biol Interact*. 2015;226:58–71. doi:10.1016/j.cbi.2014.11.016
56. Mothes E, Faller P. Evidence that the principal CoII-binding site in human serum albumin is not at the N-terminus: implication on the albumin cobalt binding test for detecting myocardial ischemia. *Biochemistry*. 2007;46(8):2267–2274. doi:10.1021/bi061783p
57. Chibber S, Ahmad I. Molecular docking, a tool to determine interaction of CuO and TiO2 nanoparticles with human serum albumin. *Biochem Biophys Rep*. 2016;6:63–67. doi:10.1016/j.bbrep.2016.03.004
58. Azizi M, Ghourchian H, Yazdian F, Dashtestani F, AlizadehZeinabad H. Cytotoxic effect of albumin coated copper nanoparticle on human breast cancer cells of MDA-MB 231. *PLoS One*. 2017;12(11):e0188639. doi:10.1371/journal.pone.0188639
59. Treuel L, Malissek M, Gebauer JS, Zellner R. The influence of surface composition of nanoparticles on their interactions with serum albumin. *ChemPhysChem*. 2010;11(14):3093–3099. doi:10.1002/cphc.201000174
60. Capomaccio R, Jimenez IO, Colpo P, et al. Determination of the structure and morphology of gold nanoparticle–HSA protein complexes. *Nanoscale*. 2015;7(42):17653–17657. doi:10.1039/C5NR05147A
61. Konar S, Sen S, Pathak A. Morphological effects of CuO nanostructures on fibrillation of human serum albumin. *J Phys Chem B*. 2017;121(51):11437–11448. doi:10.1021/acs.jpcb.7b08432
62. Roudbaneh SZK, Kahbasi S, Sohrabi MJ, et al. Albumin binding, antioxidant and antibacterial effects of cerium oxide nanoparticles. *J Mol Liq*. 2019;296:111839. doi:10.1016/j.molliq.2019.111839
63. Horev-Azaria L, Kirkpatrick CJ, Korenstein R, et al. Predictive toxicology of cobalt nanoparticles and ions: comparative in vitro study of different cellular models using methods of knowledge discovery from data. *Toxicol Sci*. 2011;122(2):489–501. doi:10.1093/toxsci/kfr124
64. Colognato R, Bonelli A, Ponti J, et al. Comparative genotoxicity of cobalt nanoparticles and ions on human peripheral leukocytes in vitro. *Mutagenesis*. 2008;23(5):377–382. doi:10.1093/mutage/gen024
65. Rajiv S, Jerobin J, Saranya V, et al. Comparative cytotoxicity and genotoxicity of cobalt (II, III) oxide, iron (III) oxide, silicon dioxide, and aluminum oxide nanoparticles on human lymphocytes in vitro. *Hum Exp Toxicol*. 2016;35(2):170–183. doi:10.1177/0960327115579208

66. Chandrasekaran R, Yadav SA, Sivaperumal S. Phytosynthesis and characterization of copper oxide nanoparticles using the aqueous extract of beta vulgaris L and evaluation of their antibacterial and anticancer activities. *J Clust Sci*. 2020;31(1):221–230. doi:10.1007/s10876-019-01640-6
67. Jayarambabu N, Akshaykranth A, Venkatappa Rao T, Venkateswara Rao K, Rakesh Kumar R. Green synthesis of Cu nanoparticles using Curcuma longa extract and their application in antimicrobial activity. *Mater Lett*. 2020;259:126813. doi:10.1016/j.matlet.2019.126813
68. Lallo da Silva B, Caetano BL, Chiari-Andréo BG, Pietro RCLR, Chiavacci LA. Increased antibacterial activity of ZnO nanoparticles: influence of size and surface modification. *Colloids Surf B Biointerfaces*. 2019;177:440–447. doi:10.1016/j.colsurfb.2019.02.013
69. El-Sayed SM, Amer MA, Meaz TM, Deghiedy NM, El-Shershaby HA. Microstructure optimization of metal oxide nanoparticles and its antimicrobial activity. *Measurement*. 2020;151:107191. doi:10.1016/j.measurement.2019.107191
70. Chang EL, Simmers C, Knight DA. Cobalt complexes as antiviral and antibacterial agents. *Pharmaceuticals*. 2010;3(6):1711–1728. doi:10.3390/ph3061711
71. Alahmadi N, Betts J, Cheng F, et al. Synthesis and antibacterial effects of cobalt–cellulose magnetic nanocomposites. *RSC Adv*. 2017;7(32):20020–20026. doi:10.1039/C7RA00920H
72. Alsharaeh E, Mussa Y, Ahmed F, Aldawsari Y, Al-Hindawi M, Sing GK. Novel route for the preparation of cobalt oxide nanoparticles/reduced graphene oxide nanocomposites and their antibacterial activities. *Ceram Int*. 2016;42(2):3407–3410. doi:10.1016/j.ceramint.2015.10.135